processes

MDPI

Article

Model Predictive Control of Common Ground PV Multilevel Inverter with Sliding Mode Observer for Capacitor Voltage Estimation

Kelwin Silveira [1], Felipe B. Grigoletto [1,*], Fernanda Carnielutti [2], Mokhtar Aly [3], Margarita Norambuena [4] and José Rodriguez [3]

[1] Laboratory of Power Electronics and Control (LAPEC), Federal University of Pampa (UNIPAMPA), Av. Tiarajú, 810, Alegrete 97546-550, RS, Brazil; kelwinsilveira.aluno@unipampa.edu.br
[2] Power Electronics and Control Research Group (GEPOC), Federal University of Santa Maria (UFSM), Av. Roraima 1000, Santa Maria 97105-900, RS, Brazil; fernanda.carnielutti@ufsm.br
[3] Facultad de Ingeniería, Arquitectura y Diseño, Universidad San Sebastián, Bellavista 7, Santiago 8420524, Chile; mokhtar.aly@uss.cl (M.A.); jose.rodriguezp@uss.cl (J.R.)
[4] Electrical Engineering Department, Universidad Tecnica Federico Santa Maria, Valparaiso 2390123, Chile; margarita.norambuena@usm.cl
* Correspondence: felipegrigoletto@unipampa.edu.br

Abstract

Transformerless inverters have received significant attention in solar photovoltaic (PV) applications. The absence of low-frequency transformers contributes to improved efficiency and reduced size compared to other topologies; however, there are concerns about leakage currents. The common ground (CG) connection in PV inverters is an attractive solution to this issue, as it generates a constant common-mode voltage and theoretically eliminates the leakage current. In this context, multilevel CG inverters can eliminate the leakage current while achieving high-quality output voltages. Nonetheless, achieving simultaneous control of the grid current and inner capacitor voltages can be challenging. Furthermore, controlling the capacitor voltages in multilevel inverters requires feedback from measurement sensors, which can increase the cost and may affect the overall reliability. To address these issues, this paper proposes a model predictive controller (MPC) for a CG multilevel inverter with a reduced number of sensors. While conventional MPC uses a classical multi-objective technique with a single cost function, the proposed method avoids the use of weighting factors in the cost function. Additionally, a sliding-mode observer is developed to estimate the capacitor voltages, and an incremental conductance-based maximum power point tracking (MPPT) algorithm is used to generate the current reference. Simulation and experimental results confirm the effectiveness of the proposed observer and MPC strategy.

Keywords: transformerless inverters; model predictive control; MPPT; multilevel inverters; observer

check for updates

Academic Editor: Mohd Azlan Hussain

Received: 9 August 2025
Revised: 8 September 2025
Accepted: 10 September 2025
Published: 17 September 2025

Citation: Silveira, K.; Grigoletto, F.B.; Carnielutti, F.; Aly, M.; Norambuena, M.; Rodriguez, J. Model Predictive Control of Common Ground PV Multilevel Inverter with Sliding Mode Observer for Capacitor Voltage Estimation. *Processes* **2025**, *13*, 2961. https://doi.org/10.3390/pr13092961

Copyright: © 2025 by the authors. Licensee MDPI, Basel, Switzerland. This article is an open access article distributed under the terms and conditions of the Creative Commons Attribution (CC BY) license (https://creativecommons.org/licenses/by/4.0/).

1. Introduction

Renewable energies are gaining ever more importance in the energy market share. In the last decade, photovoltaic generation systems had a significant worldwide expansion [1]. New converter technologies and topologies were developed to improve the generation from the PV source. Among them, transformerless topologies stand out for enabling compact inverter designs that typically offer low cost and high conversion efficiency [2].

However, grid-connected transformerless inverters face challenges related to the presence of leakage currents.

The galvanic connection between the inverter and the grid forms a resonant circuit composed of the parasitic capacitances of the PV panels, the grounding impedance, and the output filter [2]. The common-mode voltage generated by the inverter can excite this circuit, leading to leakage currents, that must be limited in order to reduce power losses, electromagnetic interference [3], and to ensure human and equipment protection. To mitigate leakage currents, inverter topologies and modulation strategies have been proposed in the literature [4–11]. Among transformerless topologies, the common-grounded (CG) configuration represents an effective solution for mitigating leakage currents. In this topology, the negative terminal of the PV string is directly connected to the neutral point of the grid, which is grounded. As a result, the parasitic capacitances are bypassed, and the leakage current is theoretically eliminated [4,5].

The mitigation of leakage currents can also be achieved through specifically designed modulation strategies and controllers. Often, linear approaches such as proportional–integral (PI) or proportional–resonant (PR) controllers are used. However, due to the technological development of microprocessors and digital signal processors, it has become possible to apply alternative control methods to improve the quality of the output voltages and currents, as well the overall inverter performance [12–20]. Among these methods, Finite Control Set Model Predictive Control (FCS-MPC) has emerged as a promising approach, as it can efficiently perform multivariable control, while inherently accounting for system nonlinearities and constraints in its formulation [12].

FCS-MPC approaches have been successfully applied to CG inverter topologies [21]. For instance, [22] presents an FCS-MPC scheme for a single-phase five-level CG PV inverter, where two cost functions are implemented in a cascaded structure. The first cost function minimizes the current tracking error, while the second exploits the redundancies of the voltage vectors selected by the first stage to regulate the voltages of the inner capacitors. As a result, no weighting factors are required in the cost function, and no trade-off is needed between capacitor voltage regulation and output current control.

An MPC scheme with delay compensation is proposed in [23] for single-phase PV inverters. This method controls the output current of a dual-stage PV inverter, achieving good steady-state performance, a high output power factor, and fast transient response. In [24], an MPC strategy is presented for a single-phase H-bridge neutral-point clamped (H-NPC) PV inverter, delivering high-quality output current with unity power factor, while also regulating the DC-link voltage and mitigating leakage currents. Additional MPC approaches targeting leakage current reduction have been proposed for other single-phase PV inverter topologies, including full-bridge T-type five-level inverters [25], HERIC [26], transformerless H5 [27], flying capacitor configurations [28], and several recently introduced topologies [29–31].

Another important consideration in multilevel inverters is the reduction in voltage sensor count, which simplifies hardware implementation and reduces system cost. The sliding mode observer (SMO) is an effective technique for sensor reduction, capable of estimating unmeasurable variables in both linear [32] and nonlinear systems [33]. It has been successfully applied in various fields, including motor drives and power converters [34–39]. SMOs offer key advantages such as low estimation error and strong robustness against parameter variations [40]. The observation error forms the sliding surface of the observer, while a switching function drives the system toward this surface, ensuring accurate estimation. In the context of MPC and PV applications, some studies have incorporated SMOs for grid voltage reconstruction [41]. The estimated grid voltage is then used in the predictive model of grid-connected inverters, enhancing the control system's robustness and reliability.

Furthermore, ref. [42] presented two FCS-MPC strategies for a single-phase common-grounded (CG) five-level PV inverter. The first approach follows the classical multi-objective framework, employing a single cost function that includes both capacitor voltage and output current errors. The second approach adopts a cascaded structure with two cost functions, eliminating the need for weighting factors. In the second method, the first stage selects a switching state that minimizes the output current error, and the second stage selects among redundant vectors to minimize the capacitor voltage error. These strategies enable the reduction in voltage sensors for the capacitors from two to one.

This paper proposes a cascaded cost function model predictive controller (CCF-MPC) applied to the CG inverter proposed in [7]. In addition, a sliding mode observer (SMO) is proposed to estimate the capacitor voltages, eliminating the need for voltage sensors. The observer reduces the instrumentation complexity and implementation cost of the system. Furthermore, this presents simulation analyses and experimental results that validate the effectiveness of the proposed MPC strategy. The main contributions of this paper are summarized below:

- A predictive control strategy based on CCF-MPC is proposed, acting on both the output current and the capacitor voltages of a single-phase five-level inverter.
- A sliding mode observer (SMO) is developed to estimate the capacitor voltages, enabling the complete removal of physical voltage sensors from the system.
- The SMO is integrated into the MPC algorithm, providing accurate voltage estimation and eliminating the need for DC capacitor voltage sensors.
- An incremental conductance (INC) maximum power point tracking (MPPT) strategy is incorporated into the CCF-MPC framework.
- A comparison between the proposed CCF-MPC and the classical FCS-MPC is carried out, highlighting the benefits of the proposed approach when applied to the CG inverter.

This paper is organized as follows: Section 2 presents the modeling of the common ground (CG) five-level PV inverter. Section 3 describes both the conventional FCS-MPC and the proposed CCF-MPC approaches. Section 4 details the design of the sliding mode observer (SMO). Section 6 provides simulation results for both control strategies, along with experimental validation. Finally, Section 7 presents the conclusions regarding the proposed MPC strategies.

2. Description of the Common Ground Inverter Topology

This section presents the circuit topology and the dynamic model of the single-phase CG inverter considered in this paper. The inverter topology is shown in Figure 1 [7]. It consists of a half-bridge leg connected to the input, a switching capacitor cell, and a second half-bridge leg connected to the output [7]. The topology includes seven active switches, S_1 to S_7, and two capacitors, C_1 and C_2, which are switched in series or parallel and charged to half of the DC bus voltage. The inverter is capable of generating five output voltage levels: V_{dc}, $V_{dc}/2$, 0, $-V_{dc}/2$, and $-V_{dc}$.

The inverter switching states, along with their corresponding output voltages and capacitor currents, are summarized in Table 1. Each switch listed in Table 1 is in the on-state when its corresponding digital control signal is logic '1', and in the off-state when the signal is logic '0'. The current flowing through the two capacitors is the same in all switching states, i.e., $i_{C1} = i_{C2}$. Since the capacitors are alternately connected in series and parallel, their voltages remain balanced ($v_{C1} = v_{C2}$), requiring only a single voltage sensor for inverter operation.

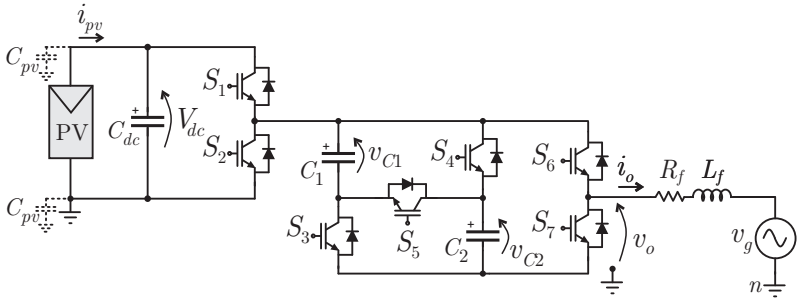

Figure 1. Single-phase five-level CG inverter topology proposed in [7] (reproduced with permission from author, JESTPE, published by IEEE, 2021).

Table 1. Inverter switching states, capacitor currents, and corresponding output voltages.

State	Gate Signals							Capacitor Current		Output Voltage
$\mathbf{v}^j$	S_1	S_2	S_3	S_4	S_5	S_6	S_7	i_{C1}	i_{C2}	v_o
$\mathbf{v}^1$	1	0	1	1	0	1	0	0	0	V_{dc}
$\mathbf{v}^2$	1	0	0	0	1	1	0	0	0	V_{dc}
$\mathbf{v}^3$	1	0	1	1	0	0	1	$i_o/2$	$i_o/2$	$V_{dc}/2$
$\mathbf{v}^4$	1	0	0	0	1	0	1	i_o	i_o	0
$\mathbf{v}^5$	0	1	1	1	0	1	0	0	0	0
$\mathbf{v}^6$	0	1	0	0	1	1	0	0	0	0
$\mathbf{v}^7$	0	1	1	1	0	0	1	$i_o/2$	$i_o/2$	$-V_{dc}/2$
$\mathbf{v}^8$	0	1	0	0	1	0	1	i_o	i_o	$-V_{dc}$

The inverter exhibits redundant switching states, where identical output voltage levels are generated by different combinations of active switches. These redundancies are advantageous for control purposes, as they introduce degrees of freedom for regulating the capacitor voltages [7]. For correct inverter operation, the switching logic must satisfy the following relationships: $S_1 = \bar{S_2}$, $S_3 = \bar{S_5}$, $S_6 = \bar{S_7}$, and $S_3 = S_4$.

Topology Modeling

The design of the FCS-MPC requires an accurate model of the inverter. The output voltage v_o can be expressed as a function of the switching states, where V_{dc} is the input DC voltage, and v_C represents the voltage across each capacitor, assuming balanced conditions ($v_{C1} = v_{C2} = v_C$). Accordingly, v_o can be written as

$$v_o = S_1 V_{dc} - S_7(1 + S_5)v_C. \tag{1}$$

The inverter is connected to the grid with an inductive filter, where L_f and R_f are the filter inductance and parasitic resistance, respectively. The equivalent model of the inverter is shown in Figure 2, and the output voltage v_o can also be expressed as

$$v_o = R_f i_o + L_f \frac{di_o}{dt} + v_g. \tag{2}$$

Substituting (1) in (2) and rearranging terms, the derivative of the output current is

$$\frac{di_o}{dt} = -\frac{R_f}{L_f} i_o - \frac{\alpha}{L_f} v_C + \frac{1}{L_f}(S_1 V_{dc} - v_g). \tag{3}$$

The capacitor voltage can be modeled as

$$\frac{dv_C}{dt} = \frac{\gamma}{C} i_o \tag{4}$$

where $\alpha = S_7(1 + S_5)$ and $\gamma = S_7(1 - 0.5S_3)$.

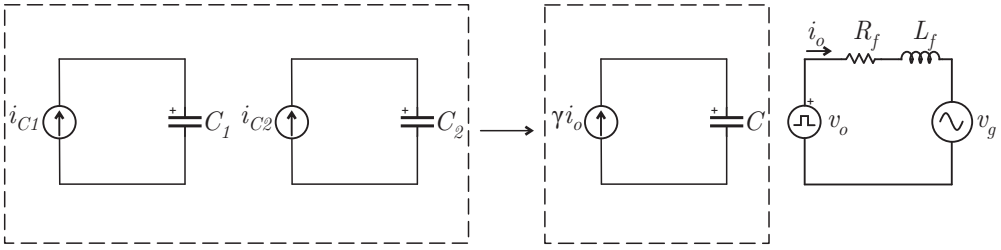

Figure 2. Equivalent model of the inverter.

The aim of the FCS-MPC is to control the output current and the capacitor voltages, so it is necessary to derive the discrete-time model to predict the variables to be controlled. Assuming a first-order approximation and a fixed sampling frequency, the Euler method is a suitable option to obtain the discrete-time model of the system [12]. Applying the Euler approximation, the discrete-time equation of the output current can be written as

$$i_o^p(k+1) = \left(1 - \frac{R_f T_s}{L_f}\right) i_o(k) - \frac{\alpha T_s}{L_f} v_C(k) + \frac{T_s}{L_f}\left(S_1 V_{dc}(k) - v_g(k)\right). \tag{5}$$

As the voltages of the capacitors C_1 and C_2 are kept balanced over the entire operating region, it is necessary to obtain the dynamic model for only one capacitor. Thus, the discrete-time model of the voltage across the capacitors is

$$v_C^p(k+1) = v_C(k) + \frac{T_s \gamma}{C} i_o(k). \tag{6}$$

3. Description of the MPC Strategies

This section describes the conventional FCS-MPC and the proposed CCF-MPC strategies.

3.1. Conventional FCS-MPC

The multi-objective FCS-MPC is characterized by multiple control objectives combined into a single cost function. Figure 3 shows the block diagram of the FCS-MPC for the considered single-phase CG multilevel inverter, where the variables $i_o(k)$ and $v_g(k)$ are measured, and $v_C(k)$ is estimated by an observer. All variables are used to predict the output current and the capacitor voltage:

$$\mathbf{x}_j^p(k+1) = f_p\left\{\mathbf{x}(k), \mathbf{v}^j\right\}, \quad \forall j \in \{1, \ldots, 8\}. \tag{7}$$

where $\mathbf{x}_{(k)} = [i_o(k) \;\; v_C(k)]^T$. Here, f_p are the both discrete model (5) for the predicted output current $i_o(k)$, and (6) for the predicted capacitor voltage.

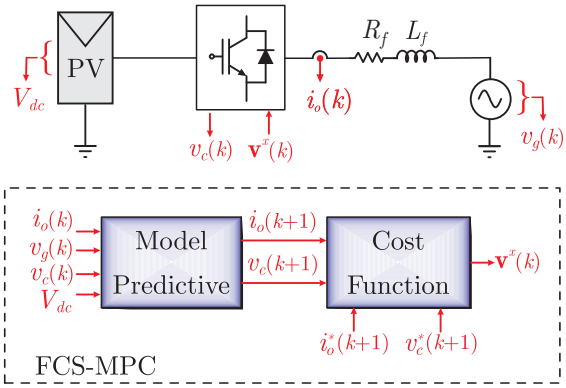

Figure 3. Block diagram of the FCS-MPC strategy.

Then, during each sampling period T_s, a cost function including the two variables is evaluated for the eight possible inverter switching states of. The j-th switching state that minimizes the cost function is selected and implemented by the inverter during T_s. The quadratic error of the variables is adopted for the cost function [43]. The weighting factors λ_1 and λ_2 assign the importance of each variable in the cost function as

$$g_i(k) = \lambda_1(i_o^*(k+1) - i_o^p(k+1))^2 + \lambda_2(v_C^*(k+1) - v_C^p(k+1))^2. \quad (8)$$

3.2. Proposed CCF-MPC Strategy

The proposed CCF-MPC employs two cascaded cost functions, where g_i and g_v are related to the optimization of the output current and the capacitor voltage [44]. Figure 4 shows the block diagram of the CCF-MPC. The two cost functions are sequentially evaluated; first, the future predicted current $i_o(k+1)$ for the i-th switching state is calculated, and the minimization of the Current Cost Function (Current CF) provides a partial solution for the state vector $\mathbf{v}_p^j(k)$. This solution is evaluated in the Voltage Cost Function block (Voltage CF) concerning $v_c(k+1)$ and the voltage reference $v_c^*(k+1)$, resulting in the final state vector $\mathbf{v}^j(k)$. Therefore, this technique does not require weighting factors, resulting in simpler formulation and reduced control effort. The following equations describe the two cost functions:

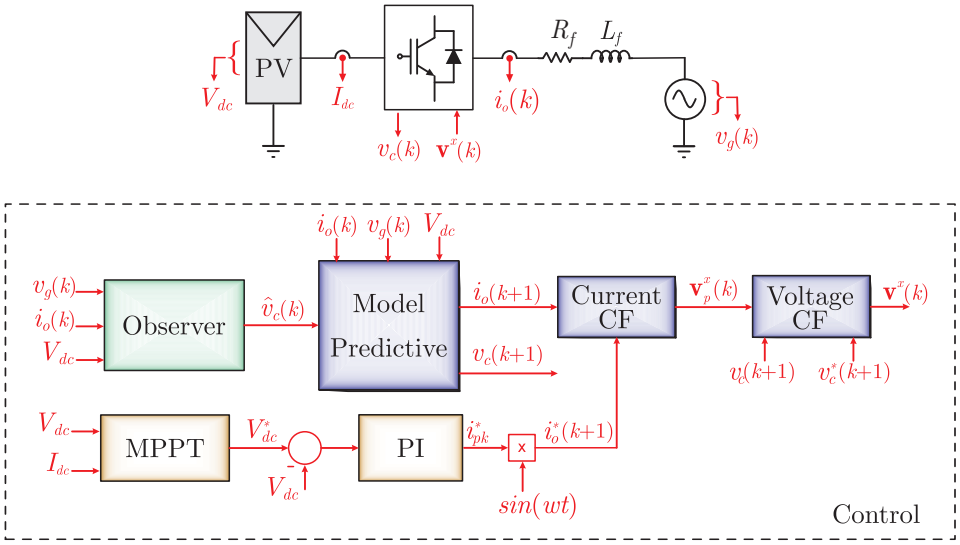

Figure 4. Block diagram of the proposed CCF-MPC strategy and the SMO observer.

$$g_i(k) = (i_o^*(k+1) - i_o^p(k+1))^2 \quad (9)$$

$$g_v(k) = (v_C^*(k+1) - v_C^p(k+1))^2. \quad (10)$$

Similarly to the FCS-MPC, for the CCF-MPC, the variables $i_o(k)$ $v_g(k)$ are measured, and the estimated $v_C(k)$ is used for the prediction of the output current and the capacitor voltage. Then, during each T_s, the cost function (9) is first evaluated for the five inverter switching states, as redundancies are not considered in this stage. From the selected switching state that minimizes (9), the cost function (10) is evaluated, selecting the redundant state that minimizes the capacitor voltage error. The redundant switching states for the voltage level V_{dc} are $\mathbf{v}^1$ and $\mathbf{v}^2$, and the redundant switching states for the voltage level zero are $\mathbf{v}^4$, $\mathbf{v}^5$, and $\mathbf{v}^6$. Finally, the selected switching vector is implemented by the inverter during T_s.

4. Sliding Mode Observer—SMO

Due to the characteristics of the MPC and inverter in both presented implementations, the elimination of the DC voltage sensor is proposed. As a result, the inverter can operate with a reduced number of sensors by employing a model that represents the behavior of capacitors C_1 and C_2.

To eliminate all capacitor voltage sensors in the inverter system, a combined approach using MPC and a SMO is proposed. Sliding Mode strategies, whether applied as observers or controllers, offer several notable advantages, including simplified design, rapid dynamic response, and robustness to parameter variations [45]. Nevertheless, SMOs also present certain limitations, such as the chattering phenomenon and increased implementation complexity in nonlinear systems. The SMO requires the execution of some steps, like the following.

The implementation of the SMO involves the following steps:

- Formulation of the state-space model for the system;
- Verification of the observability of the system;
- Definition of the sliding surface;
- Design of the observer model;
- Verification of the stability of the observer.

The space-state model that represents the dynamics of the output current, and the capacitor voltage is

$$\begin{bmatrix} \dot{i_o} \\ \dot{v_C} \end{bmatrix} = \begin{bmatrix} -\frac{R_f}{L_f} & -\frac{\alpha}{L_f} \\ \frac{\gamma}{C} & 0 \end{bmatrix} \begin{bmatrix} i_o \\ v_C \end{bmatrix} + \begin{bmatrix} \frac{1}{L_f} \\ 0 \end{bmatrix} \begin{bmatrix} S_1 V_{dc} - v_g \\ 0 \end{bmatrix}$$
$$y = \begin{bmatrix} 1 & 0 \end{bmatrix} \begin{bmatrix} i_o \\ v_C \end{bmatrix}. \tag{11}$$

To assess the observability of the system, the matrix O must be constructed. It can be derived from (11) as $O = [C^T; (CA)^T]^T$, that results in

$$O = \begin{bmatrix} 1 & 0 \\ -\frac{R_f}{L_f} & -\frac{\alpha}{L_f} \end{bmatrix}. \tag{12}$$

The observability is confirmed since $\text{rank}(O) = 2$. This assumption holds for the state vectors $\mathbf{v}^3$, $\mathbf{v}^4$, $\mathbf{v}^7$, and $\mathbf{v}^8$ since the current that flows through the capacitor in these states is non-zero (12). In the remaining vectors, there is no current flowing, and the voltage is not observable. However, because of the high switching frequency of the control method, these intervals are brief, allowing the global system to be considered observable. The variables $\hat{i_o}$ and $\hat{v_C}$ are the estimated output current and the capacitor voltage, respectively.

The sliding surface is defined as the observation error between the real measures and the observations expressed by $\tilde{i}_o = i_o - \hat{i}_o$ e $\tilde{v}_C = v_C - \hat{v}_C$. The sliding surface will force the trajectory of the system to an equilibrium point where the error is zero. Hence, the expressions of the SMO can be written as follows:

$$\frac{d\hat{i_o}}{dt} = -\frac{R_f}{L_f}\hat{i_o} - \frac{\alpha}{L_f}\hat{v_C} + \frac{1}{L_f}(S_1 V_{dc} - v_g) + k_1 sgn(\tilde{i}_o) \tag{13}$$

$$\frac{d\hat{v_C}}{dt} = \frac{\gamma}{C}\hat{i_o} + \left(\frac{\gamma}{C} - \frac{\alpha}{L_f}\right)\tilde{i}_o + k_2 sgn(\tilde{i}_o). \tag{14}$$

The gains k_1 and k_2 must be designed to result in a suitable behavior of the estimated variables. Subtracting (3) from (13) and (4) from (14), the derivative of the estimation error can be obtained:

$$\frac{d\tilde{i}_o}{dt} = -\frac{R_f}{L_f}\tilde{i}_o - \frac{\alpha}{L_f}\tilde{v}_C - k_1 sgn(\tilde{i}_o) \tag{15}$$

$$\frac{d\tilde{v}_C}{dt} = \frac{\gamma}{C}\tilde{i}_o + \left(\frac{\alpha}{L_f} - \frac{\gamma}{C}\right)\tilde{i}_o - k_2 sgn(\tilde{i}_o). \tag{16}$$

To determine the stability of the system, the Lyapunov stability theorem can be applied. A Lyapunov candidate function V can be used to demonstrate the stability of the SMO. According to the Lyapunov stability criterion, the system is stable if the condition $\dot{V} \leq 0$ is satisfied. Let us consider a Lyapunov candidate function defined in terms of the previously established sliding surface:

$$V = \frac{1}{2}(\tilde{i}_o^2 + \tilde{v}_C^2). \tag{17}$$

To infer about the stability of the system, V is derived as

$$\dot{V} = -\frac{R_f}{L_f}\tilde{i}_o^2 - k_1|\tilde{i}_o| - k_2 sgn(\tilde{i}_o). \tag{18}$$

To ensure system stability, $\dot{V}$ must be negative. Therefore, k_2 in (18) must be very small to satisfy this condition. Also, a small value for k_1 results in an oscillatory transient response in the estimated variables. On the other hand, if k_1 is very large, the estimated variables take a long time to converge. The SMO in the discrete-time domain can be written as

$$\hat{i_o}[k+1] = \left(1 - \frac{R_f T_s}{L_f}\right)\hat{i}_o[k] - \frac{\alpha T_s}{L_f}\hat{v_C}[k] + \frac{T_s}{L_f}(S_1 V_{dc}[k] - v_g(k)) + k_1 T_s sgn(\tilde{i}_o[k]) \tag{19}$$

$$\hat{v_C}[k+1] = \frac{\gamma T_s}{C}\hat{i}_o[k] + T_s\left(\frac{\gamma}{C} - \frac{\alpha}{L_f}\right)\tilde{i}_o[k] + k_2 T_s sgn(\tilde{i}_o[k]). \tag{20}$$

The estimated voltage is fed back into the MPC, eliminating the need for voltage sensors across the DC capacitors.

Stability Analysis with Nonzero Initial Conditions

Considering the derivative of the candidate Lyapunov function in (18) and assuming the sliding surface $s = |\tilde{i_o}| >= 0$, when $i_o > 0$ $(sgn(\tilde{i_o}) = 1)$, the Lyapunov derivative becomes

$$\dot{V} = -R_f/L_f s^2 - k_1 s - k_2. \tag{21}$$

Since R_f/L_f is positive and constant, with $k_1 > 0$ and $k_2 > 0$, it follows that $\dot{V} < 0$ for all $s > 0$. Therefore, any trajectory starting with $i_o(t) > 0$, for all $t >= 0$, satisfies the condition $\dot{V} <= -cV$ for some $c > 0$, ensuring exponential convergence to the origin [46]. On the other hand, when $\tilde{i_o} < 0$ $(sgn(\tilde{i_o}) = -1)$, the expression becomes

$$\dot{V} = -R_f/L_f s^2 - k_1 s + k_2. \tag{22}$$

In this case, the positive term k_2 may lead to $\dot{V} > 0$ when s is small. In this way, there is no guarantee of energy dissipation in V, as the behavior depends exclusively on the initial condition of s. To ensure stability, $k_2 << k_1$ is required.

In conclusion, for any initial condition with $\tilde{i_o} > 0$, the system remains stable and converges to zero error. However, when the initial condition is $\tilde{i_o} < 0$, the solution can be

repelled from the origin if k_2 does not satisfy the restriction $k_2 << k_1$. Therefore, the root of $\dot{V}$ is expressed as

$$s^* = \frac{-k1 + \sqrt{k_1^2 + 4\frac{R_f}{L_f}k_2}}{2\frac{R_f}{L_f}}. \tag{23}$$

Equation (23) tends to result in a very small value, and consequently the instability range will also be very small. The initial condition $\tilde{i_o} < 0$ which leads to instability will only occur if the initial condition of observer is $\hat{i_o} > i_o$.

5. Incremental Conductance-Based Maximum Power Point Tracking Strategy

Maximum power point tracking (MPPT) is one of the most critical aspects of the control strategy for power converters in grid-connected photovoltaic systems [47]. Over the years, several MPPT strategies have been proposed; however, two methods stand out in the literature due to their widespread adoption: Perturb and Observe (P&O) and INC. These two techniques have become popular mainly because of their ease of implementation, as they are generic algorithms that do not require knowledge of the specific characteristics of the photovoltaic array to operate effectively.

In this paper, the implementation of the INC strategy is adopted due to its advantages over the P&O method. Among these advantages, its ability to accurately identify the maximum power point (MPP) stands out, unlike P&O, which continues to perturb the voltage even when the system is already operating at the MPP. This characteristic allows the method to eliminate oscillations around the optimal point [48], resulting in improved system performance. Furthermore, under varying irradiance conditions [49], the INC strategy demonstrates a higher tracking efficiency compared to P&O. Despite these distinctions, some studies propose an equivalence between both methods [47,50].

The INC algorithm was proposed in [51] and is based on the search for the point at which the partial rate of change of power with respect to voltage is zero, that is, at the peak of the P–V curve:

$$\left.\frac{\partial P}{\partial V}\right|_{\substack{P=P_{mp}\\V=V_{mp}}} = 0 \Rightarrow \left.\frac{\partial (VI)}{\partial V}\right|_{\substack{I=I_{mp}\\V=V_{mp}}} = 0 \Rightarrow V_{mp}\frac{\partial I}{\partial V} + I_{mp} = 0. \tag{24}$$

The term $\frac{\partial I}{\partial V}$ represents the incremental conductance of the system, while $\frac{I_{mp}}{V_{mp}}$ corresponds to the instantaneous conductance at the maximum power point.

The INC algorithm is based on the analysis of current (ΔI) and voltage (ΔV) variations in the photovoltaic system. Initially, the algorithm checks whether there is a voltage variation. If ΔV is null, it then evaluates the current variation. If there is also no current variation $(\Delta I \approx 0)$, the system is considered to be operating at the MPP.

If a variation in ΔI is detected while ΔV remains null, then we have the following:

- If $\Delta I > 0$, the reference voltage (V_{ref}) should be increased.
- If $\Delta I < 0$, V_{ref} should be decreased.

On the other hand, if a variation in ΔV is observed, the algorithm compares the incremental conductance with the instantaneous conductance:

- If $\frac{\partial I}{\partial V} = -\frac{I}{V}$, the condition $\frac{\partial P}{\partial V} = 0$ is satisfied, indicating that the system is operating at the MPP.
- If $\frac{\partial I}{\partial V} > -\frac{I}{V}$, the operating point is to the left of the MPP, and V_{ref} should be increased.
- If $\frac{\partial I}{\partial V} < -\frac{I}{V}$, the operating point is to the right of the MPP, and V_{ref} should be decreased.

As highlighted in [52], the MPP is typically located within a region between 70% and 80% of the photovoltaic array's open circuit voltage (V_{oc}). Based on this observation, it is possible to implement the method using a variable step size, aiming to reach the MPP more quickly. In this approach, the algorithm applies a larger voltage increment when operating outside the maximum power region. Once the system enters the desired region, the step size is reduced to allow fine-tuning of the voltage.

6. Results and Discussion

6.1. Simulation Results

This section presents simulation results to evaluate the performance of the proposed CCF-MPC with a voltage observer and to compare it with the conventional FCS-MPC strategy, both applied to the single-phase CG multilevel inverter. The simulation parameters used for both MPC strategies are summarized in Table 2.

Table 2. System parameters.

Parameter	Value
Power	1 kW
Input dc-voltage (V_{dc})	260–280 V
Capacitor voltage reference (v_C^*)	130 V
Capacitance (C_1 and C_2)	3 mF
Grid Frequency	60 Hz
Grid peak voltage	155 V
Grid filter inductance (L_f)	9 mH
Grid filter resistance (R_f)	700 mΩ
Power Switches	IKW40N60D
Sampling Time	40 µs

The FCS-MPC was simulated independently of the observer, and its design requires the selection of weighting factors λ_1 and λ_2 to achieve optimal performance. These weighting factors can be empirically tuned by analyzing the total harmonic distortion (THD) of the output current and the capacitor voltage error. The capacitor voltage error is defined as $e_C = 100\%(v_C^* - \bar{v}_C)/v_C^*$ and quantifies the deviation of the average capacitor voltage from its reference value.

Figure 5 shows the influence of λ_1 on the output current THD (red curve) and the capacitor voltage error (blue curve). In this analysis, λ_2 was kept constant at 1, while λ_1 was varied from 0 to 10. Results indicate that λ_1 values between 1 and 5 yield an acceptable compromise between low THD and small voltage error. Therefore, $\lambda_1 = 3$ was selected in this work, as it offers a balanced trade-off between the output current quality and capacitor voltage regulation.

Equivalent to the FCS-MPC, the observer integrated into the CCF-MPC and also requires tuning of the parameters k_1 and k_2. These observer gains significantly affect the transient response of the estimated capacitor voltage, $\hat{v}_C$. Figure 6 illustrates the convergence behavior of $\hat{v}_C$ for three different values of k_1, namely, $k_1 = \{10, 1000, 2500\}$, with $k_2 = 1 \times 10^{-6}$ held constant. The results indicate that as k_1 increases, the dynamic response of the observer becomes slower. A suitable transient performance was observed for $k_1 = 1000$, where all simulations shown in Figure 6 exhibit a steady-state error smaller than 1×10^{-6}, which is considered acceptable for this application.

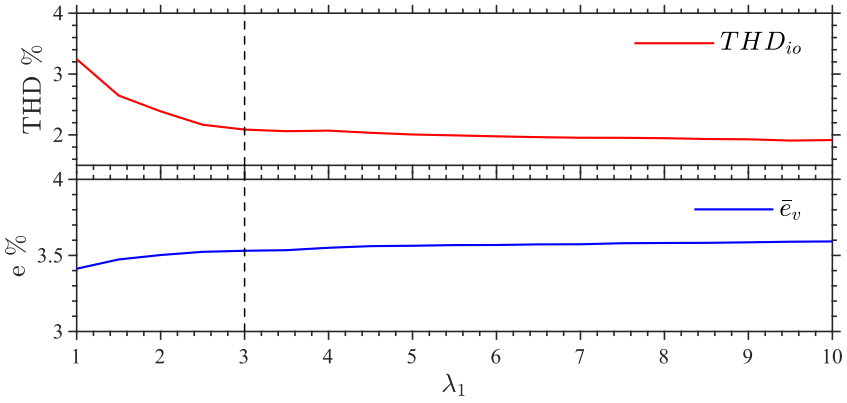

Figure 5. Output current THD and capacitor voltage error as a function of λ_1 for the FCS-MPC.

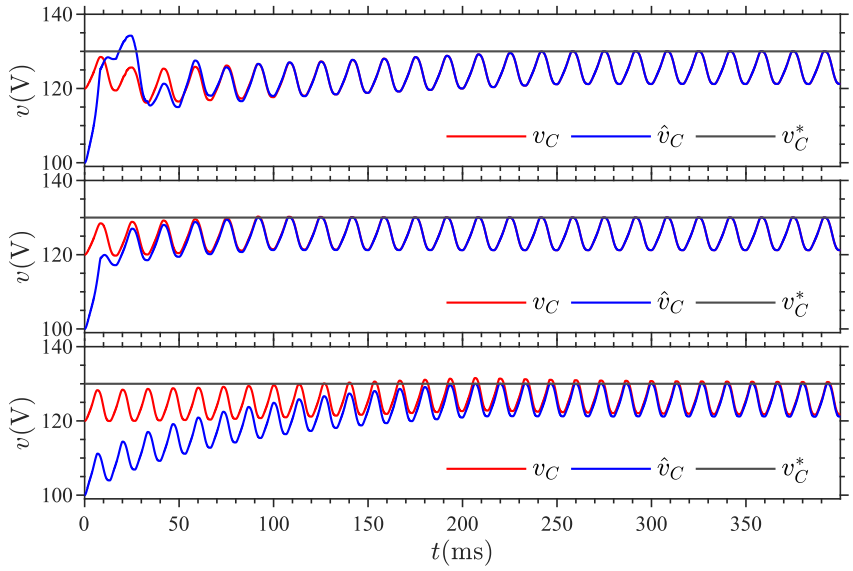

Figure 6. Convergence of $\hat{v}_C$ for the SMO and CCF-MPC. $k_1 = 10$ (**top**), $k_1 = 1000$ (**middle**) and $k_1 = 2500$ (**bottom**).

Figure 7 shows the transient response to a step change in the input DC voltage at $t = 33$ ms. The responses for the FCS-MPC and CCF-MPC strategies are depicted in Figure 7a and Figure 7b, respectively. The step causes the input voltage to change from 260 V to 270 V, which results in an increase in the capacitor voltage reference from 130 V to 135 V. Despite the voltage variation, the capacitor voltage stabilizes quickly, demonstrating the effectiveness of both MPC strategies in regulating the voltage under dynamic conditions.

Furthermore, the output current remains virtually unaffected by the input voltage step, highlighting the robustness of both controllers in maintaining stable operation under input perturbations.

Further insights are provided in Figure 8, which shows the system response to a step change in the current reference, transitioning from a leading to a lagging power factor. At $t = 105$ ms, the current reference amplitude changes from 4 A (with a leading power factor of 0) to 7 A (with a lagging power factor of 0). The responses for the FCS-MPC and CCF-MPC strategies are shown in Figure 8a and Figure 8b, respectively. In both cases, the system exhibits fast dynamic tracking of the reference current while maintaining the average capacitor voltage close to its reference value.

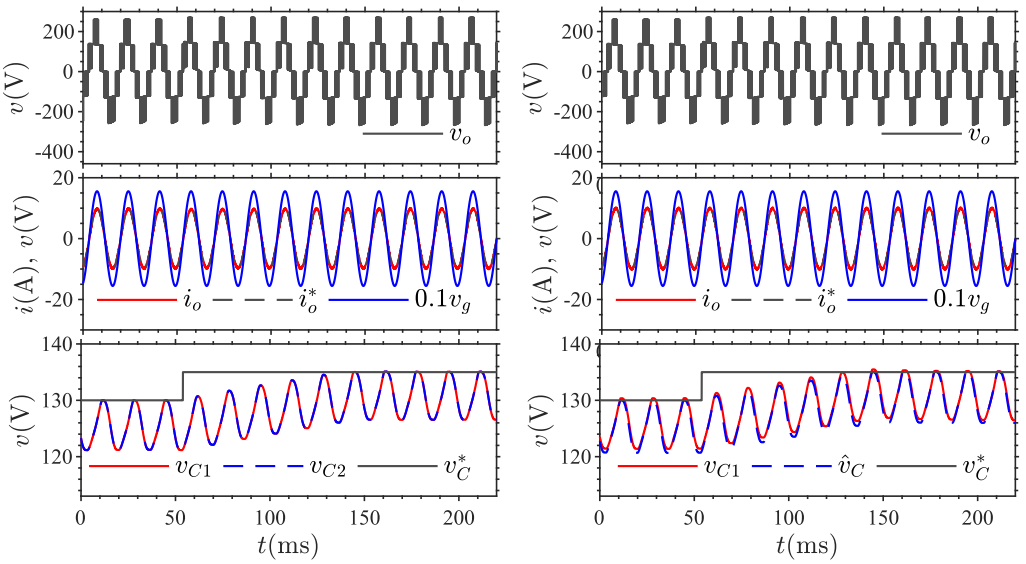

(**a**) FCS-MPC. (**b**) CCF-MPC.

Figure 7. Simulation results for a step in the dc-bus voltage reference.

These results demonstrate the capability of the controllers to promptly adapt to variations in current demand while ensuring stable voltage regulation within the system.

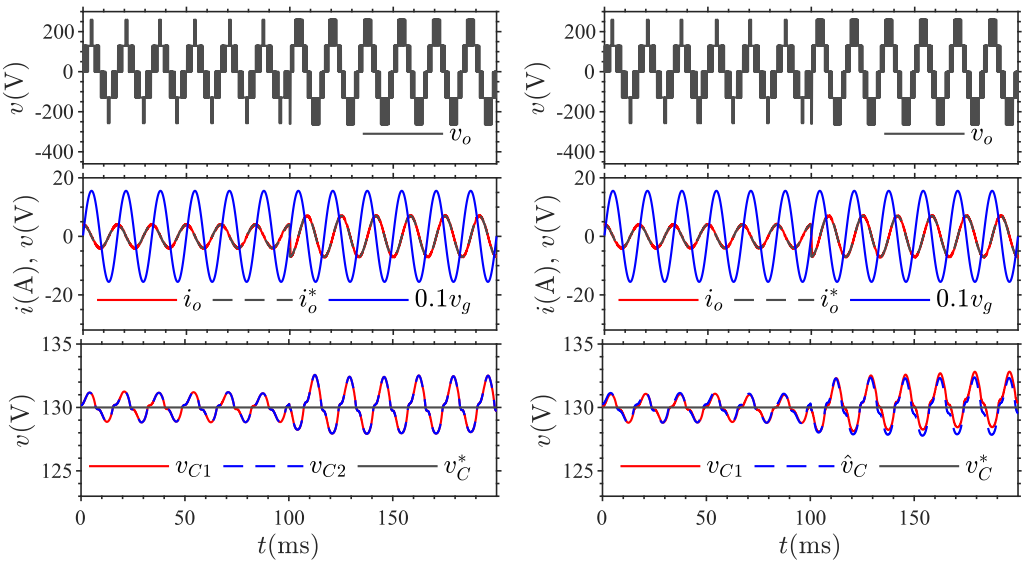

(**a**) FCS-MPC (**b**) CCF-MPC

Figure 8. Simulation results for a step in the current reference from 4 A (leading PF) to 7 A lagging PF).

To evaluate the behavior of the observer under parametric variation conditions, Figure 9 shows the impact of capacitance variation on both the capacitor voltage error and the observer voltage estimation error, defined as $\tilde{v}_C(\%) = 100(v_C - \hat{v}_C)/v_C^*$. To analyze the observer dynamics while considering the control method used in the inverter, the observer was connected to the inverter operating with FCS-MPC. Accordingly, Figure 9 presents error curves for both the CCF-MPC and the FCS-MPC, with the observer implemented in both cases.

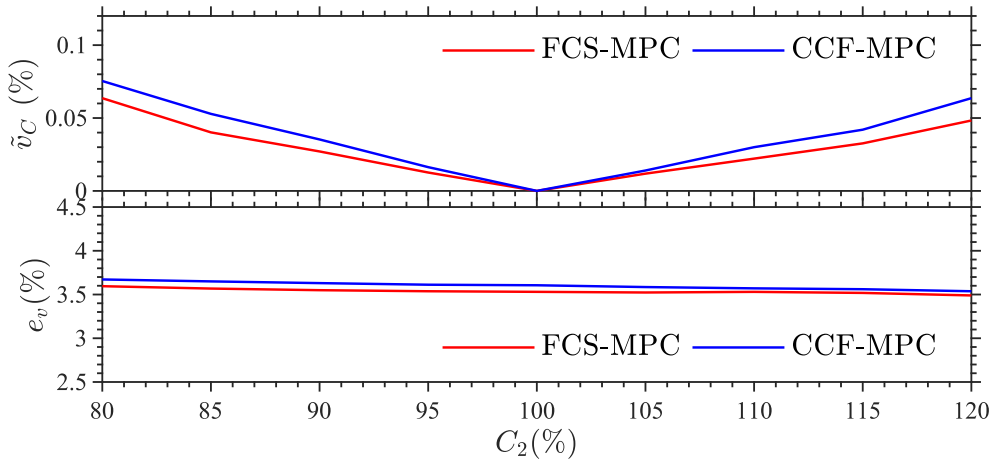

Figure 9. Impact of variation in the capacitance C_2 on the capacitor voltage error and the observer voltage estimation error for the FCS-MPC and the proposed CCF-MPC strategies.

The results indicate that the observer error is minimized when the actual capacitance matches its nominal value. Even with a capacitance variation of ±20%, the maximum observer error remains below 0.07%, demonstrating the robustness of the proposed strategy. Moreover, as expected, increasing the capacitance results in a smoother voltage profile with reduced ripple, which contributes to a decrease in e_C.

To evaluate the controller performance under parametric variations of the inductance, the same simulation procedure was carried out. The inductance was varied from 80% to 120% of its nominal value, and both the observation error percentage and the voltage tracking error were assessed. It can be noticed that the observer error remained below 0.4% even under extreme inductance conditions, while the voltage tracking error was below 4%. Therefore, the robustness of both the observer and the CCF-MPC controller can be highlighted, with performance comparable to that of the FCS-MPC as shown in Figure 10.

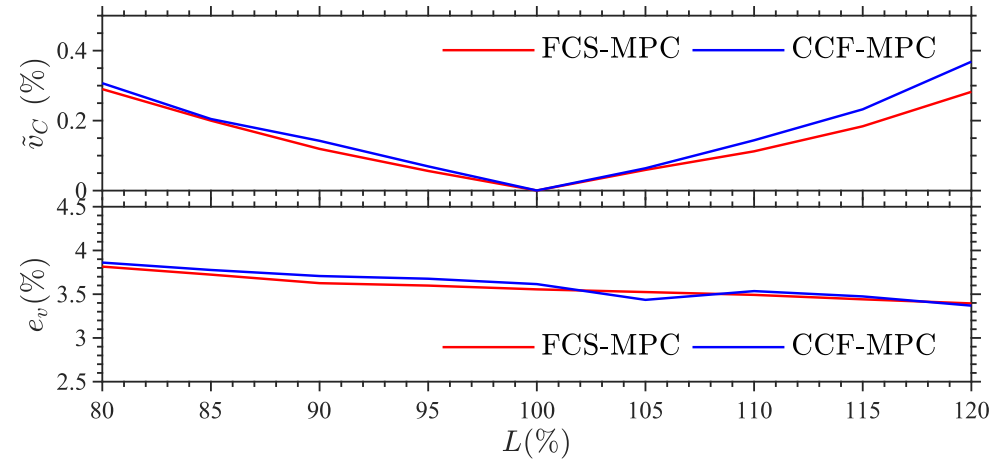

Figure 10. Impact of variation in the inductance L on the capacitor voltage error and the observer voltage estimation error for the FCS-MPC and the proposed CCF-MPC strategies.

The MPPT strategy was integrated into the simulation using the CCF-MPC. To process 1 kW, a photovoltaic array composed of 16 modules connected in parallel was designed. The selected module was the BP365, capable of supplying 65 W under maximum power conditions, with a voltage of 17.6 V and a current of 3.69 A.

As illustrated in Figure 4, the system is composed of the CCF-MPC controller operating at a sampling frequency of 20 kHz and incorporating a sliding mode observer. The controller

compares the current reference i_o^* with the measured current i_o to compute the control error. The current reference is generated by the MPPT algorithm, which uses a PI controller to determine the amplitude of i_o^* based on the voltage reference provided by the MPPT.

The power dynamics is dependent on the current control loop, which operates at high frequency, and the MPPT algorithm, which has a slower response. As proposed in [47], the sampling frequency of the MPPT algorithm is set to 100 Hz, and the cutoff frequency of PI controller is tuned to 100 Hz. Low-pass filters with a 50 Hz cutoff frequency are applied to the V_{dc} and I_{pv} signals. The MPPT step size is adaptive: a 5 V step is used outside the 70–80% range of the array's open-circuit voltage (V_{oc}), while a 1 V step is used within this range. The open-circuit voltage of the array is 353.6 V.

The simulation results include the power–voltage (P–V) curve of the photovoltaic array shown in Figure 11. Simulations were conducted at a constant temperature of 20 °C under three irradiance levels: 1 kW/m^2 (red), 0.8 kW/m^2 (blue), and 0.6 kW/m^2 (green).

Figure 12 illustrates the dynamic response of the power under grid-connected conditions. This result shows the performance of power processing during transients, such as shading and temperature changes on the P_{dc} curve. In region A, the inverter operates at 1 kW under 1 kW/m^2 irradiance and 20 °C temperature. In region B, the irradiance drops to 0.9 kW/m^2, reducing the power to 898 W. In region C, the temperature rises to 45 °C, further decreasing the input power to approximately 860 W. The grey dotted line represents the reference maximum power point P^*. The results show a fast response of the INC MPPT strategy to changes in temperature and irradiance, confirming the accuracy and effectiveness of the algorithm.

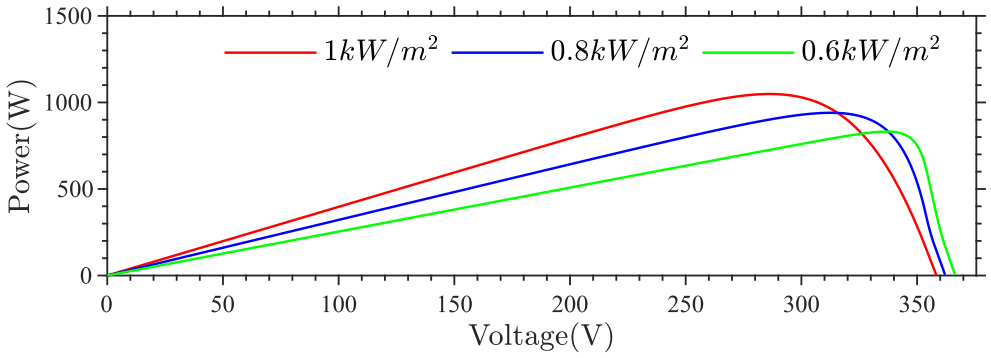

Figure 11. Photovoltaic array P×V curves.

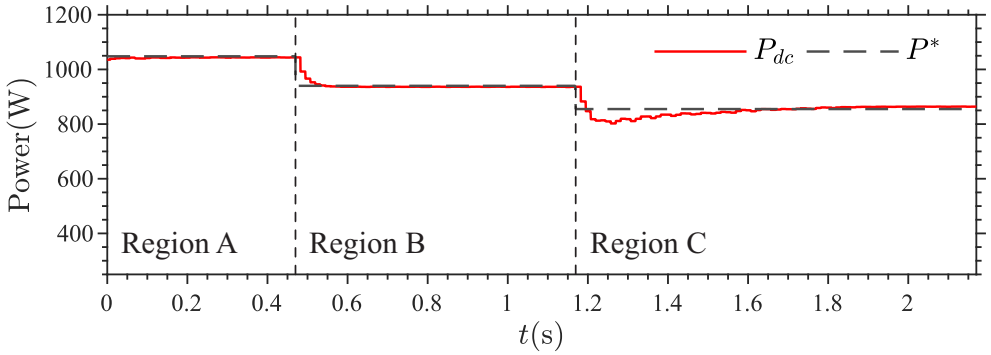

Figure 12. Transient response of the DC power at the inverter input terminals.

6.2. Power Quality Simulation Results

Simulations were carried out to evaluate the inverter performance in terms of power quality and controller robustness. The control system under evaluation consists of the MPC controller with cascaded cost functions, the MPPT strategy, and the SMO observer. Voltage sag and swell tests were performed in order to assess the controller behavior.

A voltage sag with a 12% increase above its nominal value was applied over 10 cycles of the grid voltage as shown in Figure 13a. It was observed that the output current i_o increased, reaching 16 A, approximately; the output voltage reduced to three levels, and the average voltage across the capacitors increased during this period. The recorded value of v_C^* corresponds to half of the dc-link voltage, resulting in only small variations during the operation. Regarding the THD of the output current i_o during the voltage sag, satisfactory performance was achieved, remaining at around 2.1%.

The voltage swell was applied for the same duration, with the grid voltage increasing by 12% above its nominal value as shown in Figure 13b. In this case, the inverter experienced only a minor impact on its operation, with i_o reduced to values below 15 A. Consequently, the capacitor voltage exhibited a slight drop during the swell period. Regarding the output voltage, no significant alterations were observed in its profile. With respect to the current THD, the reduction in amplitude caused a slight increase; however, it remained at an acceptable level of 2.5%.

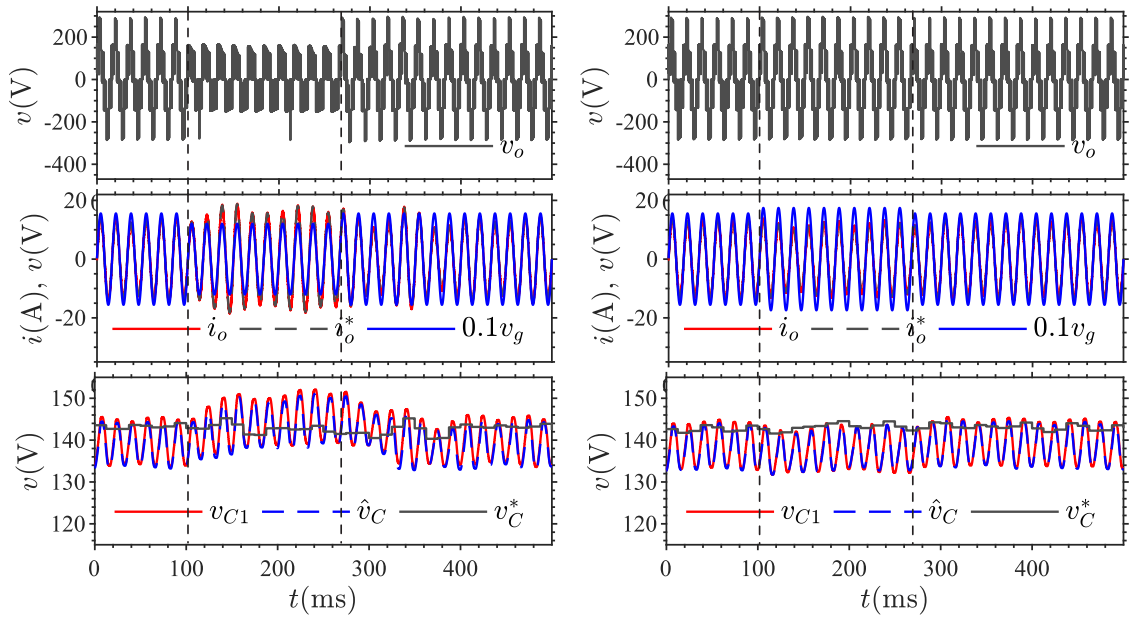

(**a**) Voltage Sag (**b**) Voltage Swell

Figure 13. Simulation results considering voltage grid disturbances. (**a**) Voltage sag. (**b**) Voltage swell.

To further evaluate the performance of the inverter under harmonic distortion in the grid, a simulation was conducted in which the grid included a significant percentage of harmonic components. The results are presented in Figure 14. Harmonics of orders 3, 5, 7, 9, 11, and 13 were introduced with amplitudes of 4%, 8%, 5%, 2.5%, 2%, and 1% of the fundamental component, respectively. Under these conditions, the control system exhibited robustness, ensuring satisfactory operation with an output current THD of 2.3%.

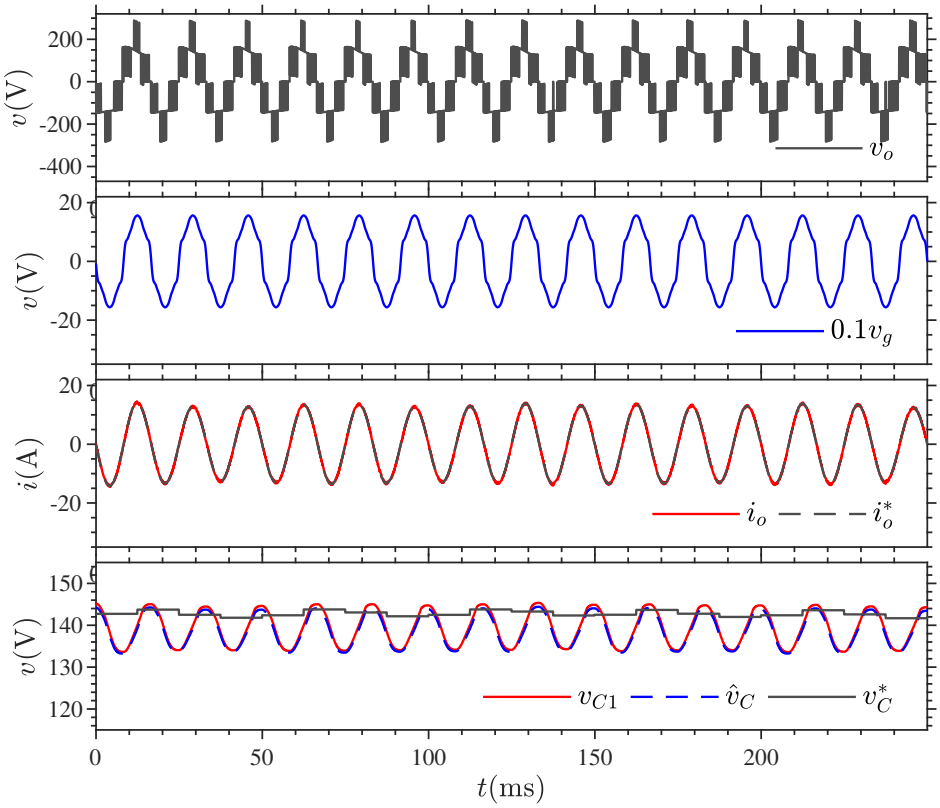

Figure 14. Simulation result of system connected in a grid with harmonic distortions.

6.3. Experimental Results

Both MPC strategies and the sliding mode observer were experimentally validated using the 1 kW prototype shown in Figure 15. A TMS320F28379D digital signal processor (DSP) from Texas Instruments was used to execute the control and observer algorithms, as well as to generate the gate signals for the inverter. The inverter's DC bus was connected to a constant voltage source, while the inverter output was connected to the electrical grid. The parameters of the experimental setup are listed in Table 2.

A digital-to-analog (D/A) output of the DSP was used to display the estimated capacitor voltage $\hat{v}_{C1}$ stored in the DSP memory. Figure 16 shows the convergence of $\hat{v}_{C1}$, starting from zero and reaching the measured capacitor voltage. The convergence behavior is consistent with the simulation results, considering an observer gain of $k_1 = 1000$.

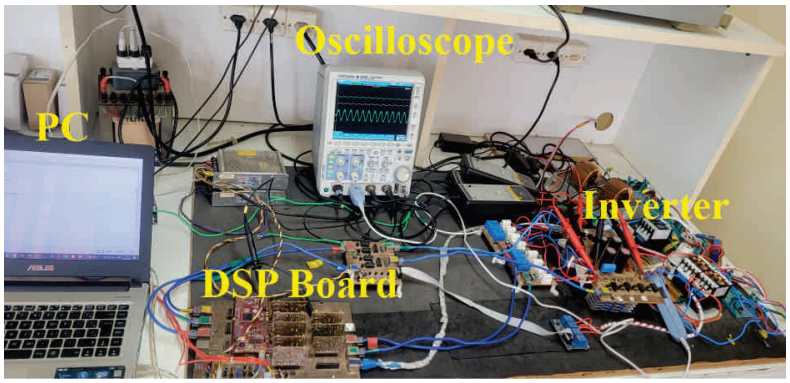

Figure 15. Photograph of the experimental setup.

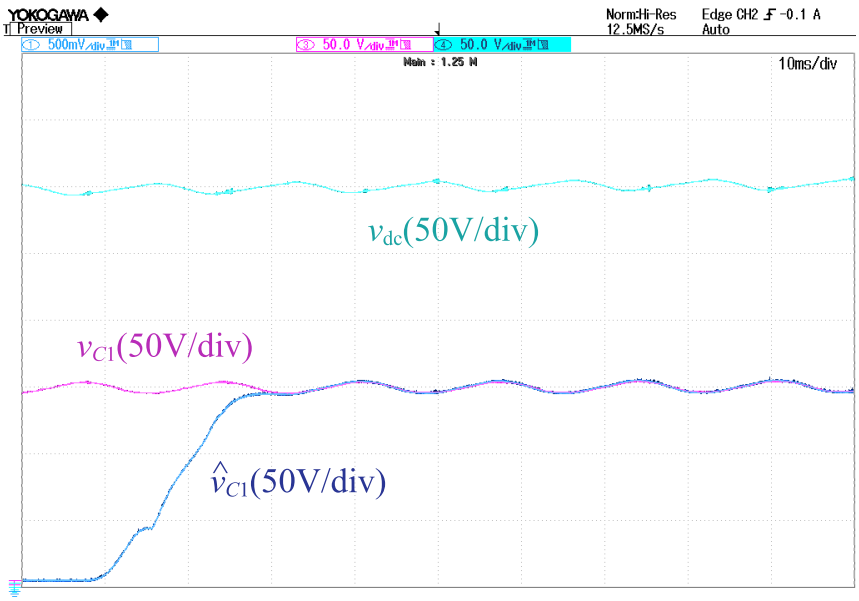

Figure 16. Experimental results: convergence of the estimated capacitor voltage, where v_{C1} is the measured capacitor voltage, $\hat{v}_{C1}$ is the estimated capacitor voltage, and V_{dc} is the input DC voltage.

The MPC strategies were experimentally tested under both steady-state and transient conditions, including a step change in the current reference. Figure 17a,b show the operation of the FCS-MPC and CCF-MPC strategies, respectively, at unity power factor with a current reference amplitude of 10 A. A very good response is observed in terms of output current tracking and capacitor voltage regulation during steady-state operation.

Figure 18a presents the transient response of the FCS-MPC strategy, while Figure 18b shows the corresponding result for the CCF-MPC strategy under the same test conditions. The current reference is changed from 4 A with power factor (PF) = 0 (leading) to 7 A with PF = 0 (lagging). Both methods demonstrate a fast dynamic response and low voltage ripple across the capacitors.

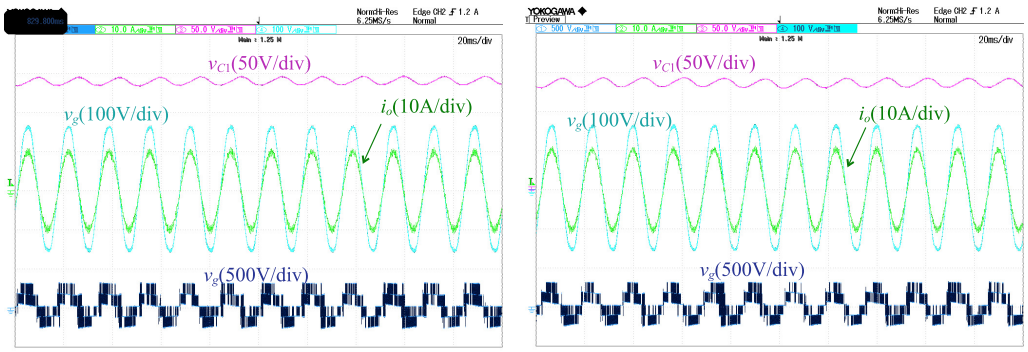

(**a**) FCS-MPC (**b**) CCF-MPC

Figure 17. Output current i_o, output voltage v_o, capacitor voltage v_{C1}, and grid voltage v_g at unity power factor operation.

Finally, Figure 19a,b display the harmonic spectrum of the output current for the FCS-MPC and CCF-MPC strategies, respectively. The total harmonic distortion (THD) of the output current is 4.35% for FCS-MPC and 4.07% for CCF-MPC.

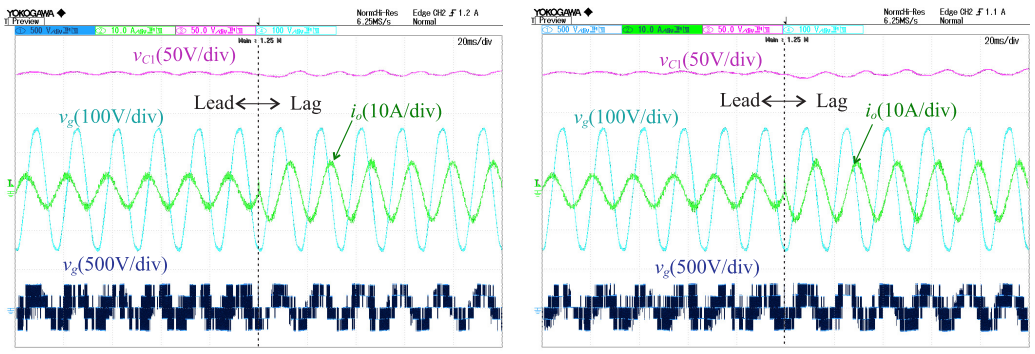

(**a**) FCS-MPC (**b**) CCF-MPC

Figure 18. Output current i_o, output voltage v_o, capacitor voltage v_{C1}, and grid voltage v_g during a step in the current reference.

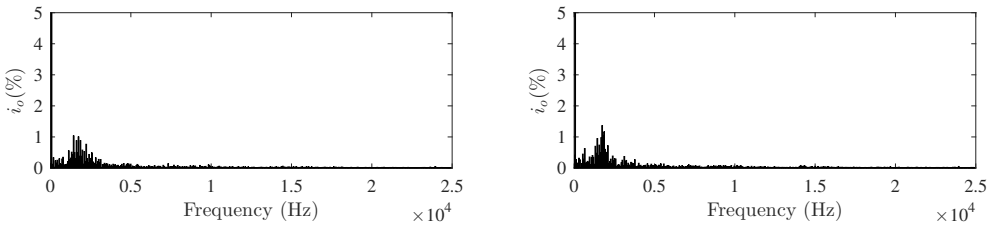

(**a**) FCS-MPC (**b**) CCF-MPC

Figure 19. Spectrum of the output current.

Table 3 summarizes a comparison between the two MPC strategies applied to the single-phase multilevel CG inverter. The FCS-MPC technique requires the selection of weighting factors, which is typically an offline and empirical process that depends on prior experience and knowledge of the controlled variables. In contrast, the CCF-MPC strategy eliminates the need for weighting factors, resulting in a more straightforward implementation.

The FCS-MPC strategy incurs a higher computational burden than the CCF-MPC, as it requires predicting both the output current and capacitor voltages for all possible switching states. In contrast, the proposed CCF-MPC approach limits its predictions to the capacitor voltages associated with redundant switching states only.

In terms of performance, the output current distortion is slightly lower with FCS-MPC, while the capacitor voltage regulation is slightly better with CCF-MPC. It is important to note that this comparison—particularly regarding total harmonic distortion (THD) and v_C error—is directly influenced by the choice of weighting factors in the FCS-MPC strategy.

Table 3. Comparison between the MPC strategies.

Features	**FCS-MPC**	**CCF-MPC**
Weighing Factor design	Yes	No
Computation Burden	3.28 µs	2.52 µs
THD_{io}(%)	4.35%	4.07%
Capacitor voltage error e_v(%)	8.5%	9.3%

6.4. Benchmark with Recent Sensorless MPC Approaches

Recent research on sensorless MPC has explored various converter topologies and estimation strategies. Table 4 summarizes representative contributions, highlighting which

sensors are eliminated, the estimation/observer used, and the notes regarding computational complexity.

Table 4. Comparison of sensorless MPC approaches.

Reference	Topology/Application	Sensors Eliminated	Observer/Strategy	Computational Notes
This work (CCF–MPC + SMO)	CG PV multilevel inverter (single-phase)	Capacitor voltages (v_{C1}, v_{C2})	Sliding-Mode Observer	2.52 µs per cycle (vs. 3.28 µs for FCS–MPC); reduced set of redundant vectors; no weighting factors
Mo et al. (2025) [53]	T-type three-level inverter	Current sensors	Two-stage selection (three-vector MPC)	Reduced prediction set; explicit aim of computational efficiency
Sarajian et al. (2025) [54]	Matrix converter-fed PMSM drive	Load current sensors	Luenberger observer	∼12% lower overhead vs. conventional schemes
Gu et al. (2025) [55]	PMSM drives	Position/ EMF sensors	SMO + simplified vector selection	Low-complexity discrete vector selection; qualitative reduction of computational burden
Nam et al. (2021) [56]	VSI with LCL filter	Grid-voltage sensors	Disturbance observer	No CPU time reported; stability and robustness focus
Nam et al. (2023) [57]	Grid-connected inverter	Grid-voltage sensors	Observer-based	Complexity not reported; disturbance rejection focus
Sharida et al. (2023) [58]	T-type rectifier	Grid-voltage sensors	Full-state observer + RLS	Qualitative: low computational burden; adds open-switch fault tolerance
He et al. (2021) [59]	Packed-U-Cell inverter (PUC)	Grid-voltage sensor	Input observer + RLS	HIL validation; complexity not quantified
Wang et al. (2022) [60]	PWM rectifier	DC bus voltage sensor	SMO + ESO observer	Robust estimation under sensor faults; complexity not quantified

From this survey, three trends can be identified:

1. **Targeted sensors:** Grid-voltage sensors are the most common target in two-level LCL inverters and rectifiers [56–60]. Load-current sensors are eliminated in certain PMSM drive strategies [53,54], while internal capacitor–voltage sensors are addressed uniquely in this work, relevant for PV-based multilevel topologies.
2. **Computational burden reporting:** Only a few studies provide explicit data—e.g., Sarajian (2025) reports a 12% reduction, and Gu (2025) uses simplified vector selection. Most sensorless MPC works emphasize robustness and stability without CPU timing. Our work is distinctive in providing measured execution times (in µs) and explicitly analyzing complexity reduction through the design of the control algorithm.
3. **Additional features:** Some works combine sensorless MPC with fault tolerance [58] or robust disturbance rejection [57,60], highlighting how sensorless strategies can yield benefits beyond sensor reduction.

Conclusion of Benchmark: The proposed CCF–MPC with SMO complements the existing literature by (i) eliminating capacitor–voltage sensors in PV multilevel inverters, (ii) demonstrating lower execution time quantitatively, and (iii) maintaining THD and capacitor–voltage balance comparable to conventional MPC.

7. Conclusions

This paper proposed a model predictive control (MPC) strategy applied to a single-phase common ground (CG) multilevel photovoltaic (PV) inverter with a reduced number of voltage sensors. The classical finite control set MPC (FCS-MPC), based on a single multi-objective cost function, offers flexibility through the tuning of weighting factors to meet specific control objectives. In contrast, the proposed cascaded cost function MPC

(CCF-MPC), which does not require weighting factors, simplifies the design process and results in a lower computational burden. Additionally, a sliding mode observer (SMO) was developed to estimate the capacitor voltage, allowing for complete sensor elimination in this measurement, thereby reducing system complexity and cost. Simulation and experimental results demonstrated the effectiveness of the MPC strategy in achieving fast reference tracking, low total harmonic distortion (THD) in the output current, and small capacitor voltage error. The robustness of the SMO was confirmed through parametric variation analysis. Furthermore, the incremental conductance (INC) maximum power point tracking (MPPT) algorithm exhibited a fast and accurate response to variations in irradiance and temperature. The relative error with respect to the true maximum power point was minimal as confirmed by the close agreement between P_{dc} and P^*.

Author Contributions: K.S. and F.B.G. contributed to the study conception, methodology design, formal analysis, investigation, validation, writing, review and editing. F.C., M.A., M.N. and J.R. contributed to writing, review and editing. All authors have read and agreed to the published version of the manuscript.

Funding: This study was financed in part by the Fundação de Amparo à Pesquisa do Estado do Rio Grande do Sul (FAPERGS), grant 2/2551-0000841-0; in part by the Conselho Nacional de Desenvolvimento Científico e Tecnológico (CNPq); in part by the Coordenação de Aperfeiçoamento de Pessoal de Nível Superior – Brasil (CAPES/PROEX), Finance Code 001; and in part by ANID, Chile AC3E (ANID/BASAL/AFB240002), FONDECYT Iniciacion 11230430, FONDECYT 1230250 and SERC-Chile ANID/FONDAP/1523A0006.

Data Availability Statement: The original contributions presented in this study are included in the article. Further inquiries can be directed to the corresponding author.

Conflicts of Interest: The authors declare no conflicts of interest.

Abbreviations

The following abbreviations are used in this manuscript:

CCF-MPC	Cascaded Cost Function Model Predictive Control
CG	Common Grounded
DC	Direct Current
FCS-MPC	Finite Control Set Model Predictive Control
H-NPC	H-bridge Neutral-Point Clamped
MPC	Model Predictive Control
MPP	Maximum Power Point
MPPT	Maximum Power Point Tracking
P&O	Perturb and Observe
PI	Proportional Integral
PR	Proportional Resonant
PV	Photovoltaic
SMO	Sliding Mode Observer

References

1. Xiao, H. Overview of transformerless photovoltaic grid-connected inverters. *IEEE Trans. Power Electron.* **2020**, *36*, 533–548. [CrossRef]
2. González, R.; Gubía, E.; López, J.; Marroyo, L. Transformerless single-phase multilevel-based photovoltaic inverter. *IEEE Trans. Ind. Electron.* **2008**, *55*, 2694–2702. [CrossRef]
3. *IEC62109-2*; Safety for Power Converters for Use in Photovoltaic Power Systems—Part 2: Particular Requirements for Inverters; International Standard: Geneva, Switzerland, 2011; ISBN 9782889124916. Available online: https://webstore.iec.ch/en/publication/6471 (accessed on 7 September 2025)

4. Kadam, A.; Shukla, A. A multilevel transformerless inverter employing ground connection between PV negative terminal and grid neutral point. *IEEE Trans. Ind. Electron.* **2017**, *64*, 8897–8907. [CrossRef]
5. Grigoletto, F.B. Five-Level Transformerless Inverter for Single-Phase Solar Photovoltaic Applications. *IEEE J. Emerg. Sel. Top. Power Electron.* **2020**, *8*, 3411–3422. [CrossRef]
6. Ardashir, J.F.; Ghassemi, M.; Rozmeh, B.; Blaabjerg, F.; Peyghami, S. A Five-Level Transformer-Less Grid-Tied Inverter Structure with Capacitive Voltage Divider Concept with Leakage Current Elimination. *IEEE Trans. Ind. Appl.* **2023**, *59*, 6025–6036. [CrossRef]
7. Grigoletto, F.B. Multilevel Common-Ground Transformerless Inverter for Photovoltaic Applications. *IEEE J. Emerg. Sel. Top. Power Electron.* **2021**, *9*, 831–842. [CrossRef]
8. Un, E.; Hava, A.M. A Near-State PWM Method with Reduced Switching Losses and Reduced Common-Mode Voltage for Three-Phase Voltage Source Inverters. *IEEE Trans. Ind. Appl.* **2009**, *45*, 782–793. [CrossRef]
9. Wu, X.; Tan, G.; Ye, Z.; Liu, Y.; Xu, S. Optimized Common-Mode Voltage Reduction PWM for Three-Phase Voltage-Source Inverters. *IEEE Trans. Power Electron.* **2016**, *31*, 2959–2969. [CrossRef]
10. Yu, B.; Song, W.; Guo, Y. A Simplified and Generalized SVPWM Scheme for Two-Level Multiphase Inverters with Common-Mode Voltage Reduction. *IEEE Trans. Ind. Electron.* **2022**, *69*, 1378–1388. [CrossRef]
11. Heo, G.; Park, Y.; Lee, J.; Ju, S. Vector-Splitting Method to Reduce Common-Mode Voltages in Two-Level Inverters for Grid Connection. *IEEE Trans. Ind. Electron.* **2021**, *68*, 11044–11052. [CrossRef]
12. Kouro, S.; Perez, M.A.; Rodriguez, J.; Llor, A.M.; Young, H.A. Model predictive control: MPC's role in the evolution of power electronics. *IEEE Ind. Electron. Mag.* **2015**, *9*, 8–21. [CrossRef]
13. Kwak, S.; Mun, S.K. Model Predictive Control Methods to Reduce Common-Mode Voltage for Three-Phase Voltage Source Inverters. *IEEE Trans. Power Electron.* **2015**, *30*, 5019–5035. [CrossRef]
14. Yu, B.; Song, W.; Guo, Y.; Li, J.; Saeed, M.S.R. Virtual Voltage Vector-Based Model Predictive Current Control for Five-Phase VSIs with Common-Mode Voltage Reduction. *IEEE Trans. Transp. Electrif.* **2021**, *7*, 706–717. [CrossRef]
15. Karasala, C.; Panindra, K.V.; Kumar, A.P.; Ganjikunta, S.K. Model Predictive Control of PVGCI for Reducing Common Mode Voltage and Switching Frequency. *IEEE J. Emerg. Sel. Top. Power Electron.* **2023**, *11*, 3064–3075. [CrossRef]
16. Liu, C.; Du, C.; Xing, X.; Jiang, Y.; Zhang, R.; Li, X.; Zhang, C. Leakage Current Suppression of Transformerless 5L-ANPC Inverter with Lower Ripple Model Predictive Control. *IEEE Trans. Ind. Appl.* **2022**, *58*, 6297–6309. [CrossRef]
17. Liu, T.; Chen, A.; Qin, C.; Chen, J.; Li, X. Double Vector Model Predictive Control to Reduce Common-Mode Voltage Without Weighting Factors for Three-Level Inverters. *IEEE Trans. Ind. Electron.* **2020**, *67*, 8980–8990. [CrossRef]
18. Guo, L.; Jin, N.; Gan, C.; Luo, K. Hybrid Voltage Vector Preselection-Based Model Predictive Control for Two-Level Voltage Source Inverters to Reduce the Common-Mode Voltage. *IEEE Trans. Ind. Electron.* **2020**, *67*, 4680–4691. [CrossRef]
19. Lee, J.H.; Lee, J.S.; Moon, H.C.; Lee, K.B. An Improved Finite-Set Model Predictive Control Based on Discrete Space Vector Modulation Methods for Grid-Connected Three-Level Voltage Source Inverter. *IEEE J. Emerg. Sel. Top. Power Electron.* **2018**, *6*, 1744–1760. [CrossRef]
20. Guo, L.; Zhang, X.; Yang, S.; Xie, Z.; Cao, R. A Model Predictive Control-Based Common-Mode Voltage Suppression Strategy for Voltage-Source Inverter. *IEEE Trans. Ind. Electron.* **2016**, *63*, 6115–6125. [CrossRef]
21. Aly, M.; Carnielutti, F.; Norambuena, M.; Yaramasu, V.; Kouro, S.; Rodriguez, J. Model Predictive Control Method for Flying Capacitor Five-Level Commonly-Grounded Photovoltaic Inverter. In Proceedings of the 2021 IEEE 12th Energy Conversion Congress & Exposition-Asia (ECCE-Asia), Singapore, 24–27 May 2021; IEEE: Singapore, 2021; pp. 1003–1008.
22. Aly, M.; Carnielutti, F.d.M.; Grigoletto, F.B.; Silveira, K.d.O.; Norambuena, M.; Kouro, S.; Rodriguez, J. Predictive Control of Common-Ground Five-Level PV Inverter Without Weighting Factors and Reduced Computational Burden. *IEEE J. Emerg. Sel. Top. Power Electron.* **2023**, *11*, 4772–4783. [CrossRef]
23. Chatterjee, A.; Mohanty, K.; Kommukuri, V.S.; Thakre, K. Design and experimental investigation of digital model predictive current controller for single phase grid integrated photovoltaic systems. *Renew. Energy* **2017**, *108*, 438–448. [CrossRef]
24. Rojas, C.A.; Aguirre, M.; Kouro, S.; Geyer, T.; Gutierrez, E. Leakage Current Mitigation in Photovoltaic String Inverter Using Predictive Control with Fixed Average Switching Frequency. *IEEE Trans. Ind. Electron.* **2017**, *64*, 9344–9354. [CrossRef]
25. Aly, M.; Ahmed, E.M.; Shoyama, M. An improved model predictive controller for highly reliable grid connected photovoltaic multilevel inverters. In Proceedings of the 2017 IEEE International Telecommunications Energy Conference (INTELEC), Gold Coast, QLD, Australia, 22–26 October 2017; pp. 450–455.
26. Bighash, E.Z.; Sadeghzadeh, S.M.; Ebrahimzadeh, E.; Yang, Y.; Blaabjerg, F. A novel model predictive control for single-phase grid-connected photovoltaic inverters. In Proceedings of the 2017 IEEE Energy Conversion Congress and Exposition (ECCE), Piscataway, NJ, USA, 1–5 October 2017; pp. 461–467.
27. Babqi, A.J.; Yi, Z.; Shi, D.; Zhao, X. Model Predictive Control of H5 Inverter for Transformerless PV Systems with Maximum Power Point Tracking and Leakage Current Reduction. In Proceedings of the IECON 2018—44th Annual Conference of the IEEE Industrial Electronics Society, Washington, DC, USA, 21–23 October 2018; pp. 1860–1865. [CrossRef]

28. Ding, H.; Li, M.; Wang, W. Leakage Current Suppression Method Based on Optimal Switching Sequence Model Predictive Control for Flying Capacitor Three-Level Inverter. In Proceedings of the 2023 IEEE International Conference on Predictive Control of Electrical Drives and Power Electronics (PRECEDE), Wuhan, China, 16–19 June 2023; pp. 1–6. [CrossRef]
29. Jiang, L.; Chen, Y.; Xiong, J.; Zhao, P. An Auxiliary Power Supply Based Nine Switch Photovoltaic Grid-Tied (AP-H9) Inverter Using Model-Free Predictive Control. In Proceedings of the 2022 5th International Conference on Power and Energy Applications (ICPEA), Guangzhou, China, 18–20 November 2022; pp. 92–97. [CrossRef]
30. Motwani, J.K.; Routray, A.; Chaudhari, N.K.; Kumar Singh, R.; Mahanty, R. Optimized Predictive Control of Hybrid Multilevel PV Inverter with Reduced Leakage Current. In Proceedings of the 2020 IEEE Energy Conversion Congress and Exposition (ECCE), Detroit, MI, USA, 11–15 October 2020; pp. 328–333. [CrossRef]
31. B, U.K.R.; Narasimharaju, B.; Babu, S.M. Model Predictive Algorithm for a New High Gain Transformer-Less Inverters with Leakage Current Elimination. In Proceedings of the 2021 International Conference on Communication, Control and Information Sciences (ICCISc), Idukki, India, 16–18 June 2021; Volume 1, pp. 1–4. [CrossRef]
32. Haskara, I.; Ozguner, U.; Utkin, V. On variable structure observers. In Proceedings of the 1996 IEEE International Workshop on Variable Structure Systems. -VSS'96-, Online, 5–6 December 1996; pp. 193–198. [CrossRef]
33. Drakunov, S.; Utkin, V. Sliding mode observers. Tutorial. In Proceedings of the 1995 34th IEEE Conference on Decision and Control, Online, 13–15 December 1995; Volume 4, pp. 3376–3378. [CrossRef]
34. Djemai, M.; Boukhobza, T.; Barbot, J.; Thomas, J.; Poullain, S. Rotor speed and flux nonlinear observer for speed sensorless induction motors. In Proceedings of the 1998 IEEE International Conference on Control Applications (Cat. No. 98CH36104), Online, 4 September 1998; Volume 2, pp. 848–852. [CrossRef]
35. Nurettin, A.; İnanç, N. High-Performance Induction Motor Speed Control Using a Robust Hybrid Controller with a Supertwisting Sliding Mode Load Disturbance Observer. *IEEE Trans. Ind. Electron.* **2023**, *70*, 7743–7752. [CrossRef]
36. Almaleki, M.; Wheeler, P.; Clare, J. Sliding Mode Observation of capacitor voltage in multilevel power converters. In Proceedings of the 5th IET International Conference on Power Electronics, Machines and Drives (PEMD 2010), Brighton, UK, 19–21 April 2010; pp. 1–6. [CrossRef]
37. da Silva, G.S.; Vieira, R.P.; Rech, C. Modified sliding-mode observer of capacitor voltages in Modular Multilevel Converter. In Proceedings of the 2015 IEEE 13th Brazilian Power Electronics Conference and 1st Southern Power Electronics Conference (COBEP/SPEC), Fortaleza, Brazil, 29 November–2 December 2015; pp. 1–6. [CrossRef]
38. Chakraborty, R.; Samantaray, J.; Dey, A.; Chakrabarty, S. Capacitor Voltage Estimation of MMC Using a Discrete-Time Sliding Mode Observer Based on Discrete Model Approach. *IEEE Trans. Ind. Appl.* **2022**, *58*, 494–504. [CrossRef]
39. Yang, H.; Zhang, Y.; Liang, J.; Gao, J.; Walker, P.D.; Zhang, N. Sliding-Mode Observer Based Voltage-Sensorless Model Predictive Power Control of PWM Rectifier Under Unbalanced Grid Conditions. *IEEE Trans. Ind. Electron.* **2018**, *65*, 5550–5560. [CrossRef]
40. Perruquetti, W.; Barbot, J.P. *Sliding Mode Control in Engineering*; CRC Press: Boca Raton, FL, USA, 2002.
41. Guo, L.; Li, Y.; Jin, N.; Dou, Z.; Wu, J. Sliding mode observer-based AC voltage sensorless model predictive control for grid-connected inverters. *IET Power Electron.* **2020**, *13*, 2077–2085. [CrossRef]
42. de Oliveira Silveira, K.; Grigoletto, F.B.; Carnielutti, F.; Aly, M.; Norambuena, M.; Rodriguez, J. Model Predictive Control for Common Grounded Photovoltaic Multilevel Inverter. In Proceedings of the 2022 14th Seminar on Power Electronics and Control (SEPOC), Santa Maria, Brazil, 12–15 November 2022; pp. 1–6. [CrossRef]
43. Kouro, S.; Cortés, P.; Vargas, R.; Ammann, U.; Rodríguez, J. Model predictive control—A simple and powerful method to control power converters. *IEEE Trans. Ind. Electron.* **2008**, *56*, 1826–1838. [CrossRef]
44. Aly, M.; Carnielutti, F.; Rodriguez, J.; Norambuena, M.; Kouro, S.; Rathore, A.K. Finite Control Set Model Predictive Control Without Weighting Factors for Common Grounded Five-Level PV Inverter. In Proceedings of the 2021 IEEE 30th International Symposium on Industrial Electronics (ISIE), Kyoto, Japan, 20–23 June 2021; IEEE: Kyoto, Japan, 2021; pp. 1–6.
45. Shtessel, Y.; Edwards, C.; Fridman, L.; Levant, A. *Sliding Mode Control and Observation*; Springer: New York, NY, USA, 2014; Volume 10.
46. Vidyasagar, M. *Nonlinear Systems Analysis*; Prentice Hall: Hoboken, NJ, USA, 2002.
47. Sera, D.; Mathe, L.; Kerekes, T.; Spataru, S.V.; Teodorescu, R. On the Perturb-and-Observe and Incremental Conductance MPPT Methods for PV Systems. *IEEE J. Photovoltaics* **2013**, *3*, 1070–1078. [CrossRef]
48. Femia, N.; Petrone, G.; Spagnuolo, G.; Vitelli, M. Optimization of perturb and observe maximum power point tracking method. *IEEE Trans. Power Electron.* **2005**, *20*, 963–973. [CrossRef]
49. Tse, K.; Ho, M.; Chung, H.H.; Hui, S. A novel maximum power point tracker for PV panels using switching frequency modulation. *IEEE Trans. Power Electron.* **2002**, *17*, 980–989. [CrossRef]
50. Kjær, S.B. Evaluation of the "Hill Climbing" and the "Incremental Conductance" Maximum Power Point Trackers for Photovoltaic Power Systems. *IEEE Trans. Energy Convers.* **2012**, *27*, 922–929. [CrossRef]
51. Wasynezuk, O. Dynamic Behavior of a Class of Photovoltaic Power Systems. *IEEE Trans. Power Appar. Syst.* **1983**, *PAS-102*, 3031–3037. [CrossRef]

52. Huynh, D.C.; Dunnigan, M.W. Development and Comparison of an Improved Incremental Conductance Algorithm for Tracking the MPP of a Solar PV Panel. *IEEE Trans. Sustain. Energy* **2016**, *7*, 1421–1429. [CrossRef]
53. Mo, R.; Yang, Y.; Chen, R.; Ni, K.; Ji, A.; Lim, C.S.; Zhang, X.; Fang, G.; Zeng, W.; Rodriguez, J. A Computationally Efficient Current-Sensorless Three-Vector Modulated Model Predictive Control with Neutral-Point Voltage Balancing for T-type Inverters. *IEEE Trans. Power Electron.* **2025**, *40*, 123–135. [CrossRef]
54. Sarajian, A.; Guan, Q.; Harbi, I.; Haghgooei, P.; Khaburi, D.A.; Kennel, R.; Wheeler, P.; Rodriguez, J. Efficient Current-Sensorless Model Predictive Control for Matrix Converter-Fed PMSM Drives. *IEEE Trans. Ind. Electron.* **2025**, 1–12. [CrossRef]
55. Gu, M.; Yang, Y.; Xiao, Y.; Fan, M.; Wang, Y.; Wen, H.; Lim, C.S.; Yang, H.; Rodriguez, J. Sensorless FCS-MPCC PMSM Drives With Improved Sliding Mode Observer and Low-Complexity Discrete Vector Selection: An Assessment. *IEEE Trans. Ind. Electron.* **2025**, *72*, 4567–4578. [CrossRef]
56. Nam, N.N.; Nguyen, N.D.; Yoon, C.; Lee, Y.I. Disturbance Observer-Based Robust Model Predictive Control for a Voltage-Sensorless Grid-Connected Inverter with an LCL Filter. *IEEE Trans. Ind. Electron.* **2021**, *68*, 4373–4384. [CrossRef]
57. Nam, N.N.; Nguyen, N.D.; Lee, Y.I. Model Predictive Control for a Voltage-Sensorless Grid-Connected Inverter with LCL Filter Using Lumped Disturbance Observer. *IEEE Trans. Power Electron.* **2023**, *38*, 8123–8135. [CrossRef]
58. Sharida, A.; Bayhan, S.; Abu-Rub, H.; Fesli, U. Voltage-Sensorless Open-Switch Fault-Tolerant Control of Three-Phase T-Type Rectifier. *IEEE Trans. Power Electron.* **2023**, *38*, 6721–6733. [CrossRef]
59. He, Y.; Li, P. Sensorless Control of Packed-U-Cells in Distorted Grid. In Proceedings of the 2021 3rd International Conference on Smart Power & Internet Energy Systems (SPIES), Shanghai, China, 25–28 September 2021; pp. 447–452. [CrossRef]
60. Wang, H.; Wang, X.; Zhang, Y.; Han, S.; Xiao, X. SMO-ESO-Based Voltage Sensorless Model Predictive Control for PWM Rectifier. In Proceedings of the 2022 4th International Conference on Smart Power & Internet Energy Systems (SPIES), Beijing, China, 9–12 December 2022; pp. 1046–1051. [CrossRef]

Disclaimer/Publisher's Note: The statements, opinions and data contained in all publications are solely those of the individual author(s) and contributor(s) and not of MDPI and/or the editor(s). MDPI and/or the editor(s) disclaim responsibility for any injury to people or property resulting from any ideas, methods, instructions or products referred to in the content.